Precision Clinical Medicine, 2026, **9**: pbaf038
https://doi.org/10.1093/pcmedi/pbaf038
Published: 19 December 2025
Research Article

OXFORD

Identification of factors conferring resistance to trastuzumab deruxtecan in advanced gastric cancer: a translational study from the single-arm, phase II, DESTINY-Gastric06 trial

Bohan Zhang[1,‡], Lei Zhang[2,‡], Cheng Liu[1], Tong Xie[1], Yifan Zhang[1], Xiao Wu[3], Yining Chen[3], Siyuan Cheng[1], Yang Feng[1], Yuxin Wang[1], Erke Gao[1], Hongquan Zhang[3,4], Lin Shen[5,*], Zhi Peng[5,*], Xiaofan Wei[3,4,*]

[1]Key Laboratory of Carcinogenesis and Translational Research (Ministry of Education), Department of Gastrointestinal Oncology, Peking University Cancer Hospital & Institute, Beijing 100142, China
[2]Department of medical and marketing, Burning Rock Biotech, Guangzhou 510300, China
[3]Department of Human Anatomy, Histology and Embryology, School of Basic Medical Sciences, Peking University Health Science Center, Beijing 100191, China
[4]Peking University International Cancer Institute, Peking University Health Science Center, Beijing 100191, China
[5]State Key Laboratory of Holistic Integrative Management of Gastrointestinal Cancers, Beijing Key Laboratory of Carcinogenesis and Translational Research, Department of Gastrointestinal Oncology, Peking University Cancer Hospital & Institute, Beijing 100142, China
*Corresponding authors: Xiaofan Wei, weixiaofan@bjmu.edu.cn; Zhi Peng, zhipeng@bjmu.edu.cn; Lin Shen, shenlin@bjmu.edu.cn.
‡Bohan Zhang and Lei Zhang contributed equally to this work

Abstract

Background: **Trastuzumab deruxtecan (T-DXd) has revolutionized the therapeutic landscape for HER2-positive gastric cancer (GC). However, tumor heterogeneity poses a significant challenge in overcoming T-DXd resistance. This study aimed to delineate the mechanisms underlying primary and acquired resistance to T-DXd in GC.**

Methods: **We performed single-cell RNA sequencing on GC tumor tissues from the DESTINY-Gastric06 study, including treatment-naive baseline samples and those with primary or acquired resistance to T-DXd. Dimensionality reduction and unsupervised clustering were applied to identify distinct cell clusters within the tumor tissues. High-dimensional weighted gene co-expression network analysis was employed to identify key gene modules associated with T-DXd resistance. Cell–cell communication was analyzed using CellChat. Key findings were experimentally validated through multiplex immunofluorescence, immunohistochemistry, and functional assays in cellular models.**

Results: **Weighted gene co-expression network analysis identified the red and purple modules as being strongly correlated with primary and acquired T-DXd resistance, respectively. Notably, MUC3A was upregulated in patients with primary resistance and its overexpression was identified as a potential predictor of shorter progression-free survival in response to T-DXd therapy. Moreover, cystatin C, a gene implicated in linker cleavage, was upregulated during the development of acquired resistance. Tumor microenvironment profiling revealed that T-DXd initially promoted immune-cell infiltration and enhanced antigen presentation. However, with the development of resistance, the tumor microenvironment shifted to an immunosuppressive state, characterized by reactivation of transforming growth factor-beta signaling and upregulation of programmed cell death protein-1 (PD-1).**

Conclusion: **These findings provide novel insights into mechanisms underlying T-DXd resistance and highlight potential therapeutic targets for overcoming T-DXd resistance in GC.**

Keywords: gastric cancer, trastuzumab deruxtecan, resistance

Introduction

Globally, an estimated 20 million new cancer cases and 9.7 million cancer-related deaths occur each year, with gastric cancer (GC) ranking as the fifth leading cause of cancer mortality [1]. GC is characterized by significant heterogeneity, with distinct molecular subtypes, such as HER2-positive tumors, leading to considerable variation in therapeutic responses [2]. Specifically, HER2-positive GC accounts for ∼10%–20% of advanced cases [3, 4]. While the ToGA trial established trastuzumab combined with con-

Received: 26 October 2025. **Revised:** 10 December 2025. **Accepted:** 17 December 2025

ventional chemotherapy as the first-line standard of care for HER2-positive advanced GC, patients inevitably develop drug resistance, leading to disease progression [5]. The mechanisms underlying trastuzumab resistance are heterogeneous and can be divided into on-target resistance mediated by HER2-related alterations, including ERBB2 mutations [6], HER2 epitope loss or masking [7], and intratumoral HER2 heterogeneity [8], and off-target resistance involving the activation of alternative signaling pathways (e.g. phosphatidylinositol 3-kinase/protein kinase B (PI3K/AKT) hyperactivation) [9] and metabolic reprogramming [10]. Unmet therapeutic needs remain for patients with HER2-positive GC who experience disease progression after first-line therapy, as effective treatment options are limited in clinical practice.

In the EMILIA study (registered with ClinicalTrials.gov: NCT00829166), trastuzumab emtansine (T-DM1) prolonged the survival of patients with HER2-positive breast cancer [11]. However, T-DM1 did not significantly improve the outcomes of patients with GC [12]. Various potential mechanisms of resistance to T-DM1 have been experimentally investigated, from antigen expression and recognition through internalization and degradation, to cytotoxic drug release and apoptotic regulation [13]. T-DXd is a next-generation antibody–drug conjugate (ADC) that combines a humanized HER2-targeting antibody with deruxtecan, a potent topoisomerase I inhibitor, connected through a cleavable tetrapeptide linker. The efficacy of T-DXd depends on the cleavage of its linker by lysosomal enzymes such as cathepsin B (CTSB) to release the cytotoxic payload [14, 15]. Deruxtecan works by causing double-strand DNA breaks, which ultimately lead to apoptosis and cell death [16]. In the DESTINY-Gastric01 and DESTINY-Gastric02 [17] studies, T-DXd demonstrated commendable efficacy, achieving an objective response rate (ORR) of 40.5% and 38%, respectively. In the DESTINY-Gastric06 study, a cohort of 95 Chinese patients with HER2-positive advanced GC were enrolled, and T-DXd showed an ORR of 28.8% [18]. In contrast to the limited efficacy of T-DM1 in GC, T-DXd exhibited superior antitumor activity in HER2-heterogeneous GC. Based on these findings, T-DXd has received regulatory approval in China as third-line therapy for HER2-positive GC.

Although T-DXd therapy has shown significant clinical benefits, most patients exhibit primary resistance, resulting in limited clinical efficacy. Furthermore, even among initially responsive cases, acquired resistance inevitably develops over time, ultimately compromising treatment outcomes. Intra-tumoral heterogeneity is common in HER2-positive GC. Studying the diversity of resistance-associated epithelial cells and their tumor microenvironment (TME) can reveal the how resistance develops and point to personalized treatment strategies.

In the DESTINY-Gastric06 study (NCT04989816), T-DXd demonstrated improved antitumor efficacy in Chinese patients with pretreated locally advanced or metastatic GC [19]. Moreover, we performed single-cell RNA sequencing (scRNA-seq) to investigate the molecular mechanisms underlying T-DXd resistance and to discover corresponding predictive biomarkers. In this study, we constructed a single-cell atlas to investigate T-DXd treatment in advanced GC, revealing both intertumoral heterogeneity among tumor cells and the dynamic evolution of the TME during therapy. We identified transcriptomic signatures associated with primary and acquired resistance to T-DXd and mapped the cell–cell communication networks involved in treatment response. To the best of our knowledge, this is the first single-cell resolution analysis of clinical samples to explore T-DXd resistance in GC, thereby yielding novel mechanistic insights into potential synergistic targets for T-DXd-based therapy.

Methods

Sample collection

Our samples were obtained from an open-label, single-arm, phase II clinical trial (DESTINY-Gastric06). This trial investigates the efficacy of T-DXd monotherapy in patients with HER2-expressing locally advanced or metastatic gastric adenocarcinoma or gastroesophageal junction (GEJ) adenocarcinoma who have previously undergone two or more treatment regimens. From this clinical cohort, we selected 11 samples from nine GC patients for our study. Detailed clinical information is provided in supplementary Table 1 (see online supplementary material). These tumor samples were collected at different treatment stages via endoscopic biopsy for single-cell sequencing analysis. Baseline samples refer to those collected before T-DXd treatment. Primary resistance was defined as disease progression during the initial treatment or within three cycles of treatment. Secondary resistance was defined as disease progression following an initial clinical response (partial response or complete response) to the treatment. Noteworthy, samples PRE-1, RES-1, and POST-1 are from the same patient's baseline phase, response phase, and resistance phase, respectively.

Establishment of single-cell libraries

Fresh tissue samples were collected during endoscopy procedures. These samples were then transported on ice using tissue storage solutions. scRNA-seq libraries were constructed following the Singleron Matrix® single-cell processing system. Pools were sequenced on Illumina NovaSeq 6000 with 150 bp paired-end reads.

Data alignment and quantification

Raw sequencing data were processed using Cell Ranger Software v6.0 (10 × Genomics) with the human reference genome GRCh38 v5.0.0 to generate a gene–cell count matrix. Initial data integration and quality control were performed with Seurat v4.1.0. Filtered datasets met the following criteria: (i) median of $>$ 1 000 genes per cell (to exclude low-quality cells); (ii) sequencing saturation between 60% and 90% (to ensure balanced library complexity); and $\geq$70% of reads mapped to cellular barcodes (to minimize ambient RNA contamination).

Doublet detection and filtering

Potential doublets were identified using the Scrublet package. Cells were over-clustered to compute cluster-level average doublet scores. Clusters with doublet scores $>$ 0.6 or expressing $>$1 canonical marker gene (e.g. *CD3D* for T cells and *MS4A1* for B cells) were removed to reduce technical artifacts.

Dimensionality reduction and clustering

Normalization, logarithmic transformation, and variable gene selection were performed with Scanpy v1.7.2. Principal component

analysis was applied for dimensionality reduction, followed by batch-balanced k-nearest neighbors to correct batch effects. Visualization was achieved through uniform manifold approximation and projection (UMAP).

Cell type annotation

Cell clusters were annotated using CellTypist, a machine learning-based tool, with reference to the Human Gastric Atlas, Immune Allow, and Immune All High datasets. Marker genes (e.g. *EPCAM* for epithelial cells, *PECAM1* for endothelial cells) were manually validated to refine annotations. Subtype proportions were calculated post-normalization to quantify population heterogeneity.

High-dimensional weighted gene co-expression network analysis of tumor epithelial cells

We performed high-dimensional weighted gene co-expression network analysis (hdWGCNA) to identify transcriptional co-expression modules associated with tumor epithelial cells. Tumor epithelial cells were isolated based on canonical markers (e.g. *EPCAM*, *KRT18*) and prior single-cell clustering annotations, retaining cells meeting quality thresholds (>1 000 genes/cell and mitochondrial content < 20%). To reduce sparsity, cells were aggregated into metacells using a k-nearest neighbors (KNN, $k = 25$) algorithm. A soft power threshold of 9 was selected to construct a scale-free network (scale-free fit index > 0.9), and hierarchical clustering of genes based on topological overlap matrices identified 13 distinct co-expression modules (e.g. turquoise, brown) via dynamic tree cutting. Module eigengenes representing each module's expression profile were correlated with clinical traits (treatment, response) using Spearman's correlation, with significance adjusted by Benjamini–Hochberg correction ($P < 0.05$).

Differential expression and functional enrichment

Differential gene expression genes (DEG) were defined as those with |log2(fold-change)| >0.5/0.25 and adjusted *P*-value < 0.05 (Benjamini–Hochberg correction). Gene ontology (GO), Kyoto Encyclopedia of Genes and Genomes (KEGG) pathway analysis, and gene set enrichment analysis (GSEA) were conducted using clusterProfiler v3.8.1 and GSEA v3.0.

Copy number variation inference

To delineate malignant epithelial cell dynamics across treatment phases (pre-treatment, therapy-responsive, and resistant stages), we employed the inferCNV package to analyze copy number variation (CNV) patterns using transcriptomic profiles. Epithelial cells from all three phases were integrated into a unified workflow, with non-malignant reference cells (e.g. stromal fibroblasts and immune cells from the same patient) serving as baseline controls. Gene expression matrices, chromosomal coordinates (gencode_v38), and cell annotations were processed with extreme expression values truncated to the range [–3, 3] to mitigate outlier effects. Initial CNV estimates (CNVi) were derived by applying asliding window of 100 genes across chromosomes to compute moving averages of relative expression values, minimizing gene-specific noise. Final CNV scores (CNVf) for individual cells were calculated as the sum of squared residuals across genomic windows, and cells in the top 10% of CNV score distributions were classified as malignant. To resolve clonal evolution, hierarchical clustering (ward. D2 linkage) and Leiden community detection (resolution = 1.0) were applied to group cells based on CNV profiles, enabling comparative analysis of subpopulations across treatment phases.

Cell–cell communication analysis

CellChat v1.6.0 was employed to infer ligand–receptor interactions. Interactions detected in <5 cells were excluded to minimize noise from low-abundance signals.

Cell culture and transfection

The human GC cell lines NUGC4 were provided by ATCC. Cell lines were cultured in RPMI-1640 medium from Gibco (MD, USA), supplemented with 10% fetal bovine serum (FBS) (Gibco, USA) and 1% streptomycin/penicillin (Gibco, MD, USA), under standard conditions (5% CO_2, 37°C). Cells were divided into three groups and transfected with control small interfering RNA (siRNA; Riobio) and specific siRNA (Riobio). When the cell lines reached 50–%60% confluency, transfection was performed using Lipofectamine 3000 reagent (Invitrogen, Carlsbad, CA, USA) at a concentration of 50 nM siRNA for 24 h to enhance transfection efficiency. Afterward, the transfection medium was removed, and the cells were seeded in 96-well plates at a density of 5000 cells/well. Once the cells adhered, the medium was replaced with complete medium containing T-DXd at final concentrations of 0, 0.00128, 0.0064, 0.032, 0.16, 0.8, 4, 20, 100, 500, 2500, 12 500 nM. After 72 h, cell viability was measured using CCK-8 according to the manufacturer's instructions, and viability curves were generated to calculate the half-maximal inhibitory concentration (IC50). Cell viability was calculated as follows: [(cell count on the third day with drug)−(cell count on zero day)]/[(cell count on the fourth day without drug)−(cell count on zero day)] × 100%. The cytotoxicity assay was performed in triplicate. Dose–response curves were generated with GraphPad Prism v9.0, from which IC50 values were extrapolated. Statistical significance was determined by one-way ANOVA analysis ($P < 0.05$). Cell RNA analysis was conducted on cells harvested 24 h post-seeding to determine transfection efficiency.

Immunohistochemistry

Paraffin-embedded tissue samples from the previously described clinical cohort were selected for immunohistochemistry (IHC) analysis to evaluate the expression levels of relevant molecules. Tissue sections were first deparaffinized and gradually rehydrated. To eliminate endogenous peroxidase activity and minimize non-specific staining, sections were treated with 3% hydrogen peroxide for 15 min. Then, the sections were subjected to antigen retrieval in EDTA buffer (pH 9.0) followed by three washes. Subsequently, the sections were incubated overnight at 4°C with rabbit anti-MUC3A (1:100 dilution, ab270247, Abcam). The next day, the

sections were incubated at 37°C with secondary antibody (goat anti-rabbit IgG, 1:2000 dilution, product number 7074, Cell Signaling Technology) for 60 min. The sections were stained with 3,3'-diaminobenzidine, counterstained with Mayer's hematoxylin, dehydrated, and mounted. Finally, photomicrographs were captured using an microscope. All IHC results were independently evaluated by two experienced pathologists.

Multiplex fluorescence IHC

For multiplex IHC staining (mIHC), formalin-fixed and paraffin-embedded (FFPE) tumor tissue blocks were serially sectioned into 6 mm sections. mIHC was conducted using the Akoya OPAL Polaris 7-Color Automation IHC kit (NEL871001KT) according to the manufacturer's protocol. Briefly, FFPE tissue slides were first deparaffinized in a BOND RX system (Leica Biosystems) and then incubated sequentially with primary antibodies for HER2 (CST, CST2165, 1:200), KRT8 (Abcam, ab53280, 1:1000), CST3 (Abcam, ab109508, 1:2000), CTSB (CST, CST31718, 1:1000), DAPI (Abcam, ab213363, 1:1000), and MKI67 (CST, 9027, 1:200). Negative control slides were processed with primary and secondary antibodies but without fluorophores to evaluate autofluorescence. Multiplex stained slides were scanned using a Vectra Polaris quantitative pathology imaging system (Akoya Biosciences) at 20 nm wavelength intervals from 440 nm to 780 nm with a fixed exposure time and an absolute magnification of 3200. All scans for each slide were then superimposed to obtain a single image. Multilayer images were imported to in Form v.2.4.8 (Akoya Biosciences) for quantitative image analysis.

Statistical analysis

Details of sample sizes and statistical tests used are described in the figure legends. Calculations were performed using GraphPad Prism 9.0 software. The Wilcoxon rank-sum test was employed to analyze differences between two independent groups with non-normally distributed data. Comparison among multiple groups was performed using one-way ANOVA. P values ≤ 0.05 were considered statistically significant; n.s. indicates no significance.

Results

Single-cell landscape of GC under T-DXd treatment

To elucidate the cellular landscape and molecular underpinnings associated with T-DXd resistance in GC, we procured samples from participants of the single-arm DESTINY-Gastric06 study and conducted a comprehensive scRNA-seq analysis. Biopsies were collected from four baseline samples (PRE), two primary resistance samples (PRE-R), and four acquired resistance samples (POST); detailed clinical information is presented in supplementary Table 1, see online supplementary material. In one individual (PRE-1), we additionally procured biopsy samples during the subsequent treatment response phase (RES-1) and acquired resistance phase (POST-1). In this study, we constructed a single-cell map of patients with GC before and after T-DXd treatment (Fig. 1A).

After multiple quality control and filtering steps, we retained gene expression profiles for 91 770 cells for subsequent biological analysis, which comprised 44 928 epithelial cells, 5134 stromal cells, and 41 708 immune cells. To visualize cells by treatment, treatment response, and individual subject, we applied UMAP analysis (Fig. 1B–D). Based on a cell annotation tool coupled with established cellular markers, we meticulously annotated the cellular constituents across 11 predominant categories: B cells (CD79A), CD4+ T cells (CD3D, CD4), CD8+ T cells (CD3D, CD8A), Natural killer (NK) cells (GNLY), macrophages (LYZ), monocytes (NAMPT), dendritic cells (CD74), mast cells (CPA3), fibroblasts (ACTA2, COL1A2), endothelial cells (PECAM1, VWF), and epithelial cells (EPCAM, KRT18, KRT8) (Fig. 1E and F). We also depicted the cell proportions for each group. There is no significant difference in cell proportions between the pre-treatment and treatment groups or treatment response, which may be attributed to constrained cohort size (Fig. 1G and H). These 11 cell clusters could further be subdivided into 30 clusters (Fig. 1I). Detailed information on the annotation genes for the main cell types and subtypes are shown in supplementary Figure S1A and B (see online supplementary material).

Epithelial heterogeneity and molecular networks in T-DXd-treated GC

We began by analyzing epithelial cells during T-DXd treatment in GC. The diversity in gene expression among these cancer cells likely plays a key role in resistance. By understanding the functions and interactions of these cells, we aimed to uncover the resistance mechanisms and help develop better treatments for HER2-positive GC. In this study, we employed the Leiden graph-based clustering algorithm to dissect heterogeneous subpopulations within epithelial cell populations and systematically analyzed their expression profiles and associated molecular networks during the development of drug resistance, with the aim of elucidating the potential regulatory roles of key subpopulations in tumor drug resistance mechanisms (Fig. 2A). We then evaluated the composition of these subclusters in each sample and observed that the Leiden 0 and Leiden 1 clusters emerged as the predominant cell subpopulations, constituting the majority of the tumor cells (Fig. 2B). To delineate the molecular signatures of distinct cellular subpopulations, we performed DEG analysis on the five clusters to systematically identify subpopulation-specific marker genes (Fig. 2C). The Leiden 2 cluster, characterized by high expression of proliferation-associated markers such as TOP2A and MKI67, was predominantly distributed in the pre-treatment samples. Notably, Leiden cluster 3, which was exclusively identified in patients with primary resistance, exhibited significant enrichment of genes related to lipid metabolism, fatty acid metabolism, glycosyl compound metabolism, and tumor necrosis factor response (Fig. 2D), suggesting that metabolic reprogramming may underlie T-DXd primary resistance mechanisms. This observation aligns with previous reports emphasizing the crucial role of metabolic remodeling in treatment resistance, including resistance to trastuzumab [10, 20].

Because the study included multiple subgroups, including pre- and post-treatment, as well as different resistance statuses, conventional pairwise comparisons were not enough to fully clarify the complex relationships between them. To address this limitation, we employed hdWGCNA to systematically investigate tumor cell co-expression patterns, subgroup-specific signatures,

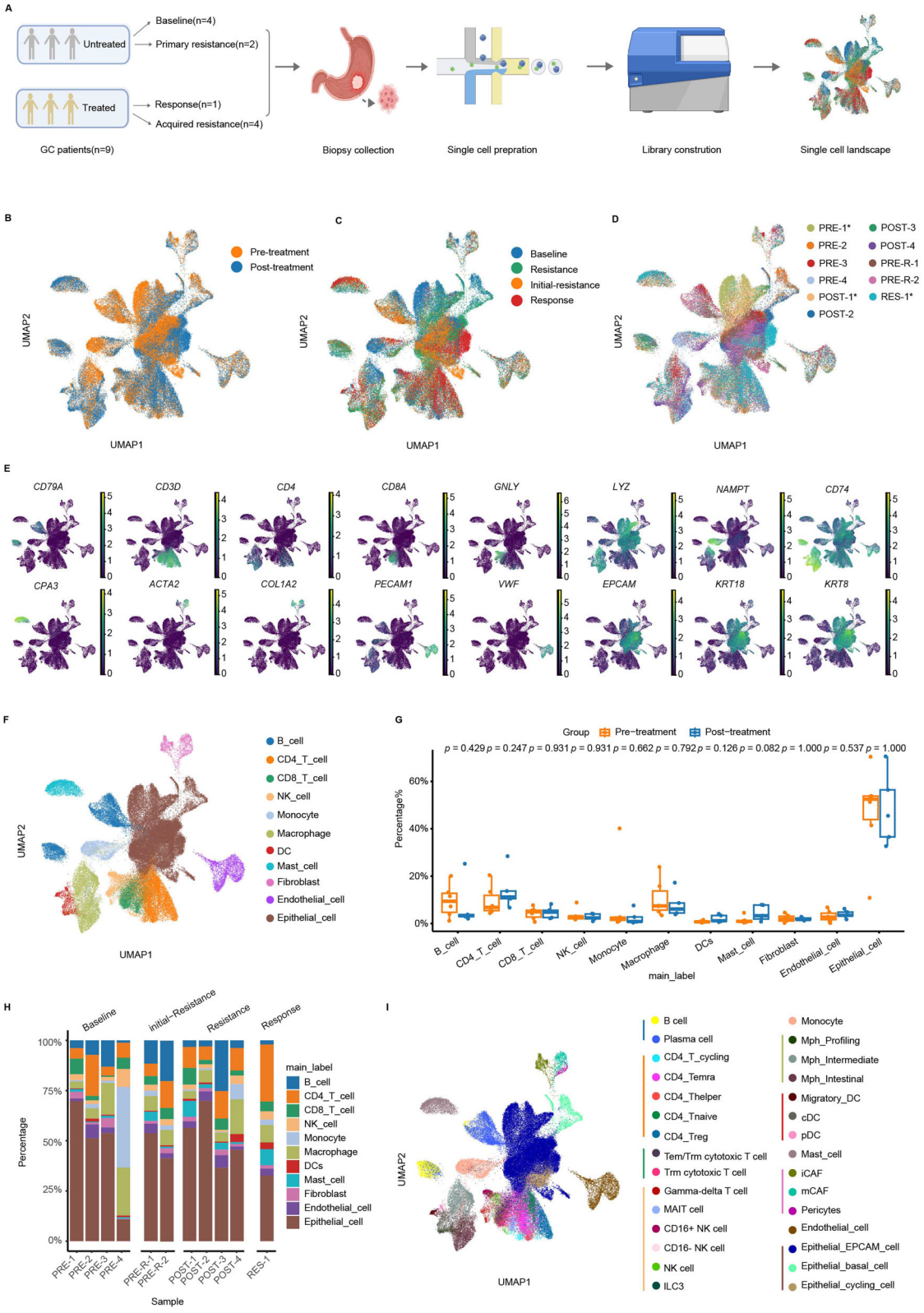

Figure 1 Single-cell landscape of GC under T-DXd treatment. (A) Diagram of the workflow for single-cell sequencing. (B–D) UMAP embedding plots of all cells colored by treatment, treatment response, and patient samples. The plot visualizes the distribution and clustering of single cells based on treatment (left), treatment response (middle), and different samples (right), with different colors representing distinct cell types. (E) Canonical marker genes for 11 major cell types, aiding in the identification and characterization of different cell populations. (F) UMAP embedding plots of all cells grouped into 11 major types. (G) Cell proportions visualized by treatment or not. This visualization provides an overview of the relative abundance of different cell types (Wilcoxon rank-sum test). (H) Cell proportions visualized by subject. This visualization provides an overview of the relative abundance of different cell types within each sample. (I) UMAP embedding plots of all cells grouped into 30 subtypes.

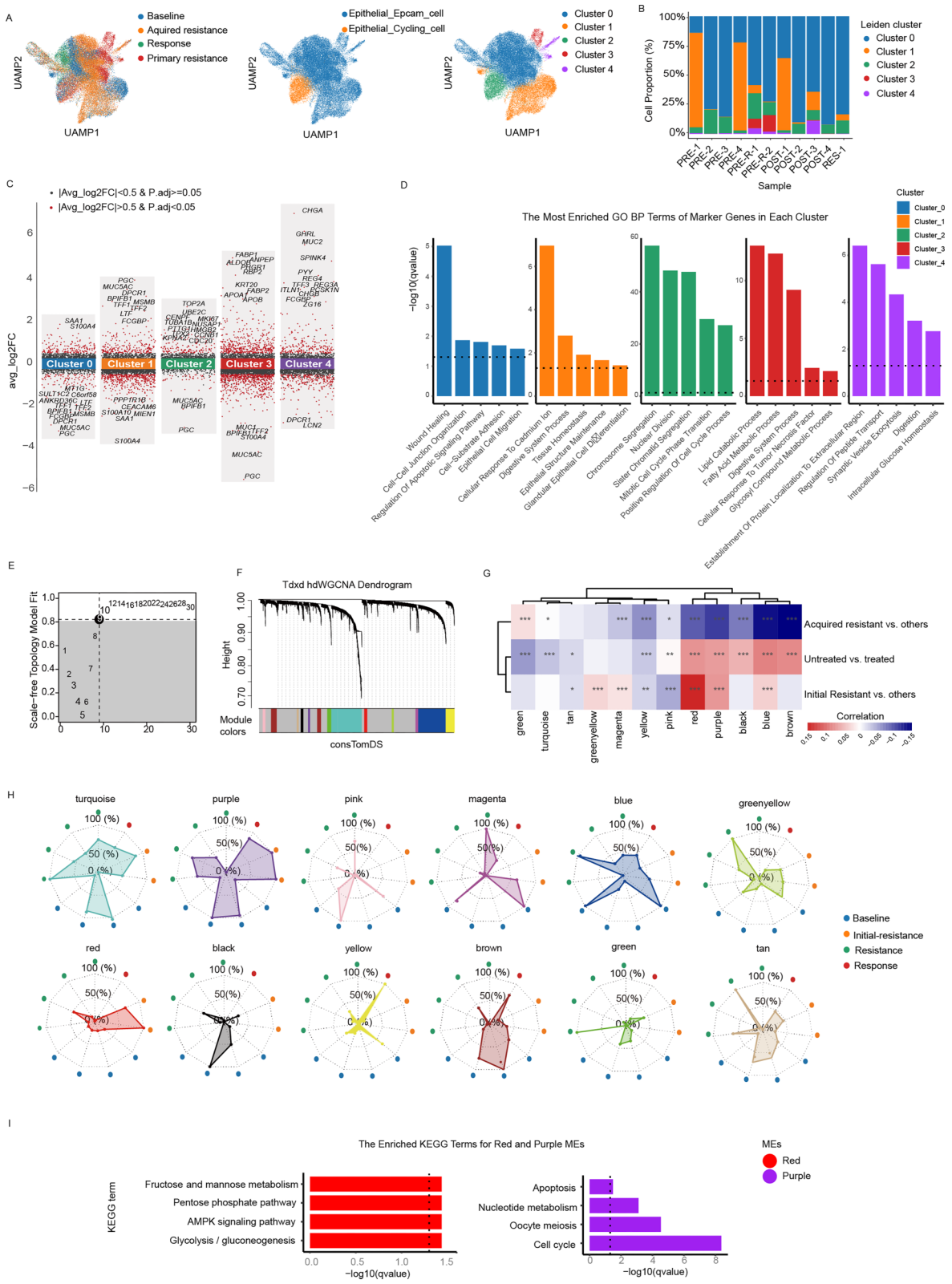

Figure 2 Epithelial heterogeneity and molecular networks in T-DXd-treated GC. (A) UMAP plots of epithelial cells stratified by groups (left), cell subtypes (middle), and Leiden clusters (right). (B) Proportional distribution of epithelial clusters across patient samples. (C) Volcano plot of DEGs between clusters (|avg_log2FC|>0.5, adjusted $P < 0.05$). Red points: significant DEGs; gray points: non-significant genes. Key cluster-specific markers are labeled. (D) Top enriched GO BP terms for each cluster. Enrichment significance is shown as −log10(q-value). (E) Scale-free topology validation for WGCNA ($R^2 = 0.80$ at soft threshold power = 9). (F) Hierarchical clustering dendrogram of co-expression modules. Colors represent distinct modules. (G) Heatmap of correlations between WGCNA modules and clinical phenotypes. Red–blue gradient indicates positive–negative correlations ($P < 0.05$). (H) Radar plot of module preservation scores across patients. (I) KEGG pathway enrichment for red and purple modules. Significance is shown as −log10(q-value).

and their correlations with clinical phenotypes. Based on the topological features of the expression matrix containing highly variable genes, the optimal soft threshold was set to nine (Fig. 2E and F, supplementary Fig. 2A, see online supplemenatary material). Twelve modules were successfully identified. The module–trait relationship was calculated by correlating each module's characteristic genes with clinical features, such as resistance status, treatment stage, and whether resistance to T-DXd was primary or acquired. This analysis was used to identify modules for downstream investigation. Through systematic analysis, we identified a significant positive correlation between the red module and primary resistance, whereas the purple module was significantly negatively correlated with acquired resistance, suggesting its potential involvement in the development of T-DXd resistance (Fig. 2G). Notably, the red module was predominantly enriched in Leiden 3 cellular clusters, whereas the purple module exhibited specific enrichment in Leiden cluster 2, which was consistent with the distribution patterns of cell clusters across samples (supplementary Fig. 2B and C). GSEA revealed that the red module was significantly enriched in pathways related to glycolysis/gluconeogenesis, the pentose phosphate pathway, fructose and mannose metabolism, and AMP-activated protein kinase (AMPK) signaling. Metabolic reprogramming is a well-established hallmark of drug resistance in tumors, including resistance to trastuzumab and T-DM1 [21, 22]. Previous studies have shown that trastuzumab-resistant epithelial cells consistently exhibit aberrant activation of glucose metabolism [22, 23]. Further investigation is required to elucidate the mechanisms of glycolytic metabolism in T-DXd resistance in GC. In contrast, the purple module was significantly associated with pathways involved in apoptosis, cell cycle regulation, nucleotide metabolism, and oocyte meiosis (Fig. 2I). These findings highlight the critical roles of the red and purple modules in drug resistance, particularly through metabolic reprogramming.

MUC3A correlates with T-DXd primary resistance and serves as a predictive biomarker for clinical outcome

To comprehensively characterize the epithelial landscape of GC patients exhibiting primary resistance to T-DXd, we systematically evaluated the expression profiles of genes within the red module across all samples. Our analysis revealed that most of these genes were highly expressed in both primary resistant samples, while some genes exhibited high expression in only one of the resistant samples (Fig. 3A). Additionally, we performed DEG analysis between baseline and primary resistant samples, focusing on genes consistently upregulated in primary resistant patients, including MUC3A, MUC17, REG1A, and FABP1 among others (Fig. 3B–D).

Members of the mucin (MUC) family, including MUC3A and MUC17, have been significantly implicated in resistance to the HER2-targeted therapy trastuzumab in breast cancer [24]. Given the limited cohort size of resistant samples in our study, we further validated these genes in the baseline samples of GC patients treated with trastuzumab from the GSE22019 dataset. We found that only MUC3A gene expression had a significant negative correlation with clinical outcomes (supplementary Fig. 3A, see online supplemenatary material). Patients with higher MUC3A expression exhibited significantly poorer progression-free survival (PFS) outcomes in GC (Fig. 3E and F). Furthermore, the tumor epithelial cells of primary resistant patients exhibited significant heterogeneity, with not all tumor cells expressing MUC3A and marked inter-sample variations in their red module scores (Fig. 3G). To investigate the biological functions of MUC3A, epithelial cells were stratified into MUC3A+ and MUC3A− subgroups. DEG analysis revealed that MUC3A may be closely associated with lipid metabolism, cell−cell junctions, and digestive processes (Fig. 3H−J). Notably, stratification by MUC3A expression levels revealed that the MUC3A+ subpopulation exhibited significantly elevated red module scores (Fig. 3K).

To assess whether MUC3A could predict survival prognosis, we performed IHC staining on tumor specimens from a Peking University Cancer Hospital cohort ($n = 29$) of the DESTINY-Gastric06 trial. We divided patients into MUC3A-low (IHC score ≤ 2) and MUC3A-high (IHC score > 2) groups and found that the MUC3A-low subpopulation had longer median PFS ($P = 0.021$; Fig. 3L) than did the MUC3A-high subgroup. To further explore the role of MUC3A in T-DXd sensitivity, we knocked down its expression in HER2-positive GC lines by siRNA. Subsequent pharmacodynamic evaluation in NUGC-4 and NCI-N87 cell models showed that the decreased MUC3A level significantly enhanced cellular sensitivity to T-DXd (Fig. 3M and N). After silencing MUC3A expression with MUC3A–specific siRNA, the binding of T-DXd to NUGC4 cells was enhanced (Fig. 3O). Above all, these findings reveal the transcriptional heterogeneity of GC epithelial cells in the initial T-DXd resistance and identify MUC3A as a key mediator of T-DXd resistance through multifunctional biological pathways. Our data indicate that MUC3A expression is a potential molecular determinant of T-DXd resistance and it can serve as an effective biomarker for enabling more precise patient stratification.

Proliferation inhibition, HER2 downregulation, and CST3 upregulation correlate with T-DXd-acquired resistance

Based on previous analyses, the purple module is closely associated with the clinical features of acquired resistance. Here, we examined the expression patterns of genes within the purple module across different sample groups. Notably, genes comprising the purple module exhibited consistently low expression levels in samples with acquired T-DXd resistance (Fig. 4A). DEG analysis of tumor epithelial cells between the acquired resistance and baseline groups demonstrated significant downregulation of HER2, accompanied by marked upregulation of CST3, ASPH, PPP1R1B, and MUC5B in acquired resistance samples (Fig. 4B and C). GSEA of the DEGs demonstrated significant inverse associations between T-DXd acquired resistance and the P53 pathway, hypoxia, G2/M checkpoint, interferon gamma, and TNFA signaling pathway. Whereas pathways in oxidative phosphorylation and adipogenesis were significantly positively correlated with T-DXd acquired resistance (Fig. 4D).

Subsequently, for patients with samples obtained simultaneously at the pre-T-DXd-treatment, treatment response, and acquired resistance stages, we further explored the transcriptional changes occurring during treatment and the development of resistance to T-DXd (Fig. 4E). Fibroblasts were used as reference cells and infer copy number variation (CNV) was employed to analyze the CNV of epithelial cells (Fig. 4F). Through clustering based on CNV, we obtained six sub-clusters excluding those in the cell-

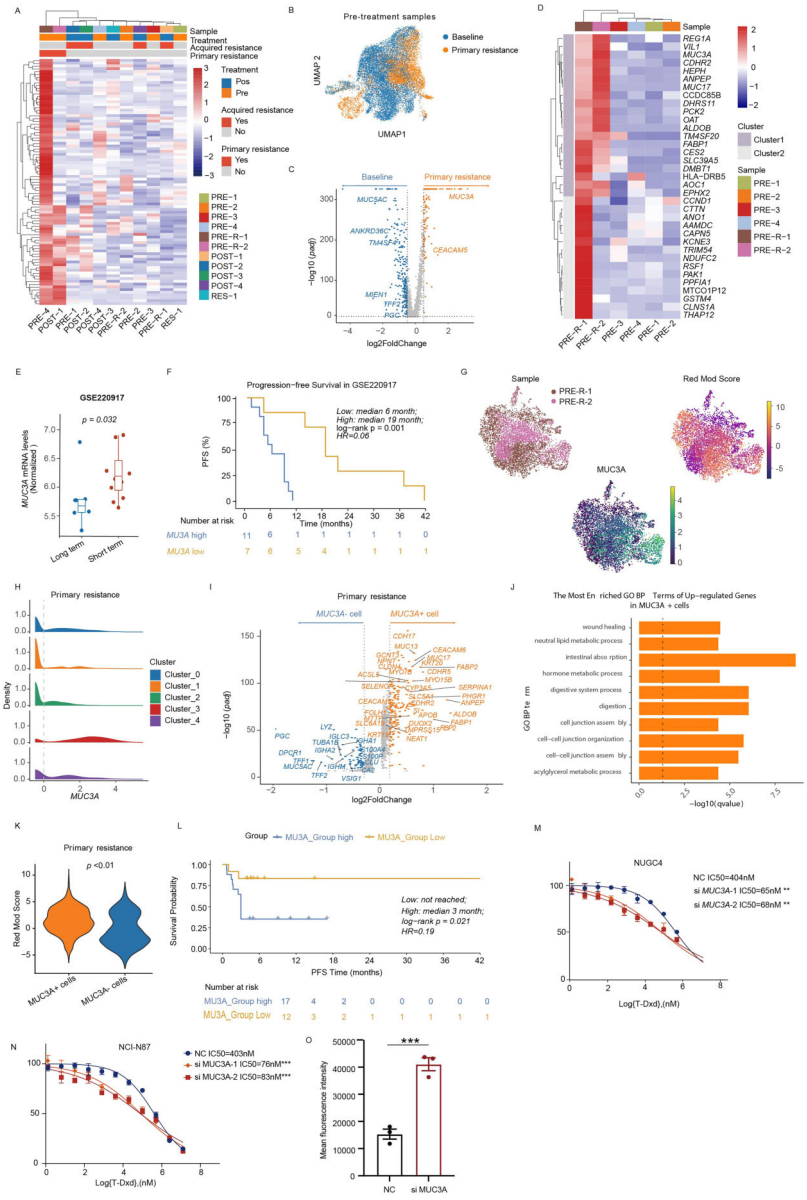

Figure 3 Molecular and clinical characterization of MUC3A+ epithelial cells in primary resistance. (A) Heatmap showing Z-scored expression of red module genes in epithelial cells among samples. Columns: individual samples; rows: genes. Color intensity (blue to red) reflects expression levels normalized per row. (B) UMAP visualization of pre-treatment epithelial cells by clinical group. (C) Volcano plot comparing gene expression between primary resistance ($n = 2$) and baseline ($n = 4$) samples. Significance threshold: $|\log_2 FC| > 0.5$ and $P < 0.05$. Yellow: upregulated in primary resistance; blue: downregulated. (D) Overlapping gene expression between red module and primary resistance signature. Heatmap displaying Z-scored expression of overlapping genes between red module and primary resistance marker genes in pretreatment samples. Columns: individual samples; rows: genes. Color intensity (blue to red) reflects expression levels normalized per row. (E) Boxplot showing MUC3A mRNA levels in baseline samples of short-term [$n = 12$, progression-free survival (PFS) < 12 months] and long-term ($n = 6$, PFS ≥ 12 months) trastuzumab responders. In the box plots, the center line corresponds to the median, box corresponds to the interquartile range. $P = 0.032$ (Wilcoxon rank-sum test). (F) Kaplan-Meier (KM) plot of PFS in trastuzumab-treated stomach adenocarcinoma patients ($n = 18$) stratified by MUC3A expression (Log-rank test). (G) UMAP annotation of primary resistance epithelial cells, Left: UMAP colored by sample identity (PRE-R-1, PRE-R-2). Right: UMAP colored by red module score (Z-score) and MUC3A expression. (H) Density plots showing MUC3A expression distribution in Leiden clusters. Cutoff at MUC3A = 0 defines MUC3A+ (≥ 0) and MUC3A− (<0) cells. (I) Volcano plot comparing gene expression between MUC3A+ and MUC3A− cells in primary resistance samples. Significance threshold: $|\log_2 FC| > 0.25$ and $P < 0.05$. Yellow: upregulated in MUC3A+; blue: downregulated. Key genes labeled. (J) Bar plot of top enriched GO biological processes for MUC3A+ upregulated genes. $-\log_{10}$(q-value) indicates enrichment significance. (K) Violin plot showing red module scores in MUC3A+ and MUC3A− cells. $P < 0.05$ (Wilcoxon rank-sum test). (L) KM plot of PFS in T-DXd-treated GC patients ($n = 29$) stratified by MUC3A expression (MUC3A high: IHC score ≥ 2). (M) Sensitivities of NUGC4 cells expressing control (blue) or MUC3A siRNAs (red/orange) to T-DXd. Statistical testing was performed by one-way ANOVA ($n = 3$ biological replications; Fisher's statistic (F) = 53.58; degrees of freedom = 8; $P = 0.0002$). (N) Sensitivities of NCI-N87 cells expressing control (blue) or MUC3A siRNAs (red/orange) to T-DXd. Statistical testing was performed by one-way ANOVA. ($n = 3$ biological replications; F = 118.4; degrees of freedom = 8; $P < 0.0001$). (O) Binding of T-DXd in NUGC4 cells transfected with control siRNA or siRNA targeting MUC3A. Quantification of T-DXd binding by mean fluorescence intensity was determined by flow cytometery ($n = 3$).

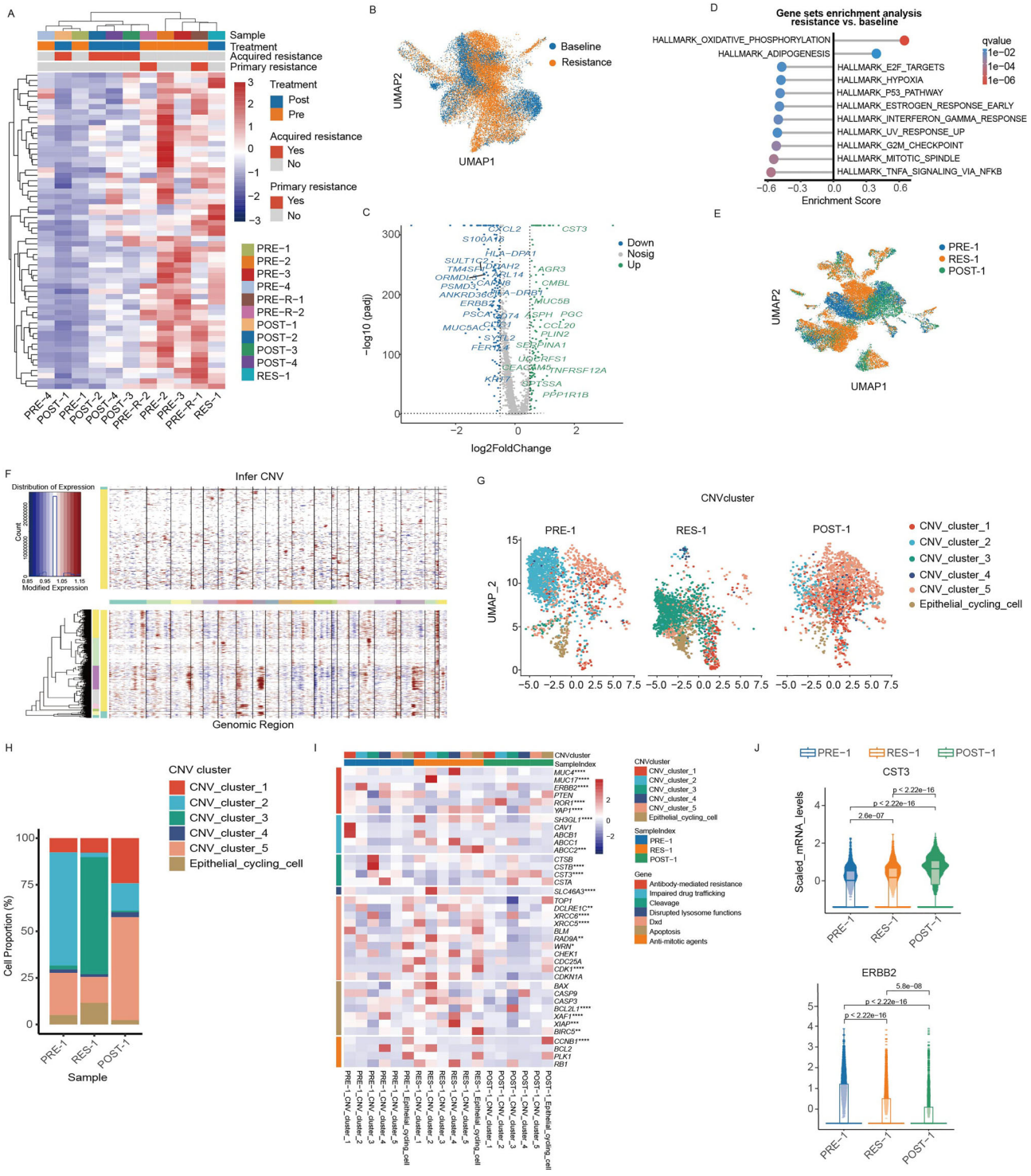

Figure 4 Temporal changes of tumor epithelial cells in patients during pre-treatment, treatment response, and acquired resistance phases. (A) Heatmap depicts expression profiles of genes within the purple module across samples, with a gradient from blue (low expression) to red (high expression). (B) UMAP visualization illustrates cellular distribution of baseline versus drug-resistant samples, color-coded by experimental group. (C) Volcano plot highlights DEGs in tumor epithelia between drug-resistant and baseline groups: green (upregulated in resistance), blue (upregulated in baseline), and gray (non-significant). (D) Bubble plot summarizes GSEA results for epithelial cells in drug-resistant versus baseline samples. (E) UMAP projection displays cell distribution from longitudinal samples (baseline, treatment-responsive phase, acquired resistance) annotated by group (top). (F) Heatmap delineates CNV characteristics in tumor epithelial cells, with mast cells and B cells as reference populations. Blue indicates depletion; red indicates amplification. (G) UMAP clusters cells based on CNV copy number, stratified by treatment phase (baseline, response, acquired resistance). (H) Stacked bar chart quantifies proportional changes of CNV clusters across treatment phases. (I) Heatmap visualizes expression of reported anti-HER2/ADC/DXd resistance-associated genes, graded from blue (low) to red (high). Significance assessed via Kruskal–Wallis test across treatment phases. (J) Box plots and beeswarm plots compare expression dynamics of CST3 and ERBB2 across baseline, response, and resistance; the Kruskal–Wallis test was performed, followed by Dunn's test for *post-hoc* analysis.

division stage (Fig. 4G). It was observed that the proportion of cells in the division stage significantly decreased during the treatment process. Meanwhile, the dominant cell population changed with the treatment. After treatment, sub-clusters 1 and 5 became the predominant cell population, while the proportion of sub-cluster 2 decreased significantly (Fig. 4H).

Next, we systematically curated resistance-associated genes reported in relation to anti-HER2 therapy, DXd-based ADCs, and cleavable linker-conjugated payloads [25, 26]. Their expression patterns were quantitatively analyzed across our cohort samples and visualized through hierarchical clustering heatmap analysis. Our findings revealed that elevated expression levels of MUC17, CST3, CDK1, SLC46A3, YAP1, and BCL2L1 are positively correlated with drug-resistant phenotypes, whereas HER2 expression exhibits significant downregulation during the acquisition of drug resistance (Fig. 4I). Further analysis of paired samples (PRE-1) revealed that CST3 expression was progressively upregulated during the treatment period, while HER2 expression demonstrated a gradual downregulation (Fig. 4J).

Acquired resistance to T-DXd: endogenous CST3 inhibits linker cleavage and impairs payload release

To characterize the dynamic expression patterns of CST3, CTSB, and HER2, we performed multiplex immunohistochemistry staining on paired samples, including matched baseline (PRE-1), treatment-responsive (RES-1), and resistant-phase (PRE-R-1) specimens. Semi-quantitative image analysis confirmed the significant downregulation of HER2 and Ki67 in KRT8+ tumor epithelial cells following T-DXd treatment, consistent with previous single-cell data. Notably, we also identified a progressive, treatment-driven expansion of the CST3+KRT8+ cell subset (Fig. 5A and B). These findings demonstrate that T-DXd effectively targets and eliminates proliferating HER2+ tumor cells via its intrinsic mechanism of action, whereas prolonged treatment induces adaptive resistance mediated by CST3 upregulation in tumor cells.

To mechanistically investigate the functions of CTSB and CST3, we established NUGC4 and NCI-N87 GC models using siRNA-mediated knockdown of CTSB and CST3. Following 72-h T-DXd exposure across a concentration gradient, dose–response curves demonstrated that CTSB-deficient cells developed acquired resistance, whereas CST3 knockdown enhanced their sensitivity to T-DXd (Fig. 5C and D). CST3 is an established endogenous inhibitor that specifically targets endolysosomal cysteine proteases, including CTSB [27, 28]. Increased CST3 expression during the resistance phase may modulate T-DXd sensitivity by inhibiting CTSB-mediated T-DXd linker cleavage. Our findings indicate that CST3 is a promising therapeutic target for overcoming resistance and optimizing treatment efficacy in GC.

Cell–cell communication in patients during pre-treatment, treatment response, and acquired-resistance phases

Beyond intrinsic signaling in epithelial cells, interactions between different cell types within the TME may also play a role in driving T-DXd resistance. To gain a deeper understanding of the cellular interactions involved, we analyzed cell–cell communication, which revealed dynamic changes in the TME during T-DXd treatment (supplementary Fig. 4A, see online supplementary material).

In the present study, we categorized the TME into 30 distinct cellular subpopulations (Fig. 6A, supplementary Fig. 1A). During the response phase, there was a notable increase in immune cell infiltration and a decrease in the proportion of epithelial cells. Concurrently, intercellular crosstalk within the TME is markedly enhanced, with macrophages emerging as the principal signal-receiving population in this communication network. In contrast, the acquired resistance phase exhibited an entirely opposite trend, characterized by a reduction in immune cell numbers, resurgence in the proportion of epithelial cells, and reconfiguration of the cellular interaction network (Fig. 6B, supplementary Fig. 4B).

CellChat-based analysis of cellular communication networks revealed dynamic alterations in intercellular signaling pathways during T-DXd treatment. The treatment-responsive phase was characterized by activation of MHC class I/II antigen presentation pathways, interferon (IFN)-γ signaling transduction, and the CXCL chemokine axis. In contrast, the development of acquired resistance was marked by pronounced reactivation of TGF-β signaling, along with activation of epidermal growth factor (EGF) and fibroblast growth factor (FGF)-mediated pathways (Fig. 6C). These alterations demonstrate that the cellular communication network underwent dynamic remodeling during T-DXd treatment. Our investigation further characterized dynamic alterations in immune checkpoint molecule (PDCD1, LAG3, TIGIT, and CTLA4) expression in T cells during treatment. Notably, PD-1 surface expression was markedly downregulated during the treatment response phase but significantly upregulated at the onset of acquired resistance (Fig. 6D).

Antigen presentation-related genes are broadly categorized into MHC class I and II molecules. Systematic analysis of their dynamic expression across baseline, treatment-responsive, and resistant phases showed a marked increase in signal intensity for both MHC class I/II during the treatment-responsive phase. In contrast, the resistance phase was characterized by significant impairment of antigen presentation, suggesting a mechanism by which tumor cells may evade immune detection (Fig. 6E, supplementary Fig. 4C).

Furthermore, the TGF-β signaling axis emerged as a critical regulatory network, showing substantial suppression during treatment response but demonstrating reactivated signaling activity within the TME during resistance progression. Mechanistic analysis identified the TGFβ1–TGFβR2 ligand–receptor pair as the dominant molecular interaction driving this pathway reactivation. This signaling axis predominantly designates T lymphocytes, B lymphocytes, and natural killer cells as the main transmitters of TGF-β signaling, while endothelial cells function as predominant signal recipients (Fig. 6F). In conclusion, these results suggest that combinatorial immunotherapy during treatment may elicit synergistic antitumor effects.

Discussion

The therapeutic landscape for HER2-positive GC is significantly constrained by the dual mechanisms of primary and acquired re-

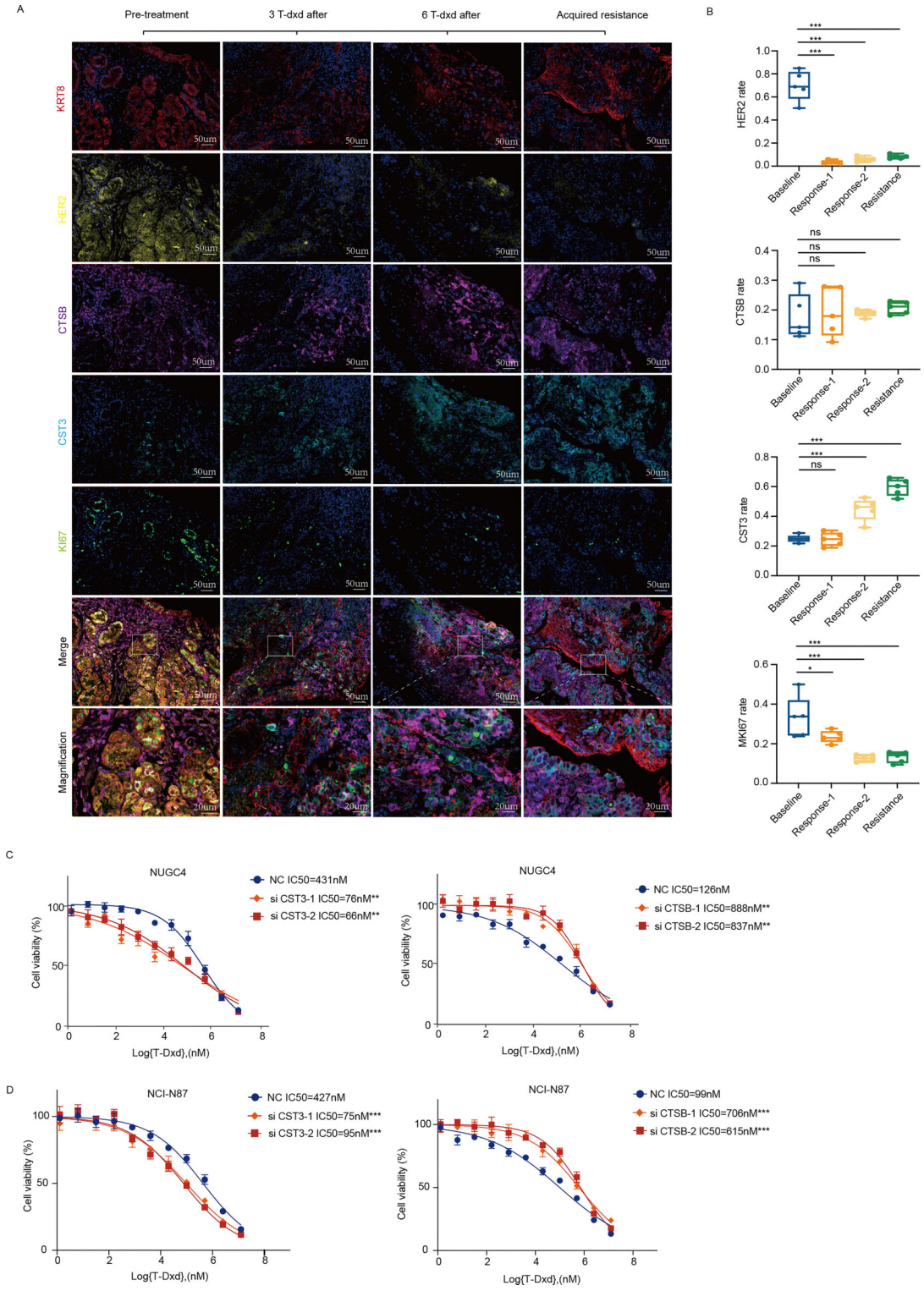

Figure 5 Endogenous CST3 inhibits linker cleavage and impairs payload release. (A) Paired samples obtained from patients who underwent biopsy. These images depict the representative images of mIHC, showcasing the expression changes of CTSB, CST3, and HER2. (B) Boxplots depicting the expression dynamics of HER2, CTSB, CST3, and MKI67 across the baseline, response, and resistance phases. For each phase, five randomly selected fields of view were quantified, and differences among groups were assessed by one-way ANOVA, followed by Tukey's HSD test. (F = 112/0.2457/48.67/14.44; degrees of freedom = 19). (C) Sensitivities of NUGC4 cells expressing control (blue) or CTSB/CST3 siRNAs (red/orange) to T-DXd. Statistical testing was performed by one-way ANOVA. CTSB ($n = 3$ biological replications; F = 18.46; degrees of freedom = 8; $P = 0.0027$). CST3 ($n = 3$ biological replications; F = 283; degrees of freedom = 8; $P < 0.0001$). (D) Sensitivities of NCI-N87 cells expressing control (blue) or CTSB/CST3 siRNAs (red/orange) to T-DXd. Statistical testing was performed by one-way ANOVA. CTSB ($n = 3$ biological replications; F = 41.74; degrees of freedom = 8; $P = 0.0003$). CST3 ($n = 3$ biological replications; F = 78.13; degrees of freedom = 8; $P < 0.0001$). Asterisks denote statistical significance (∗p < 0.05, ∗∗p < 0.01, ∗p < 0.001), and "ns" indicates not significant (p ≥ 0.05).

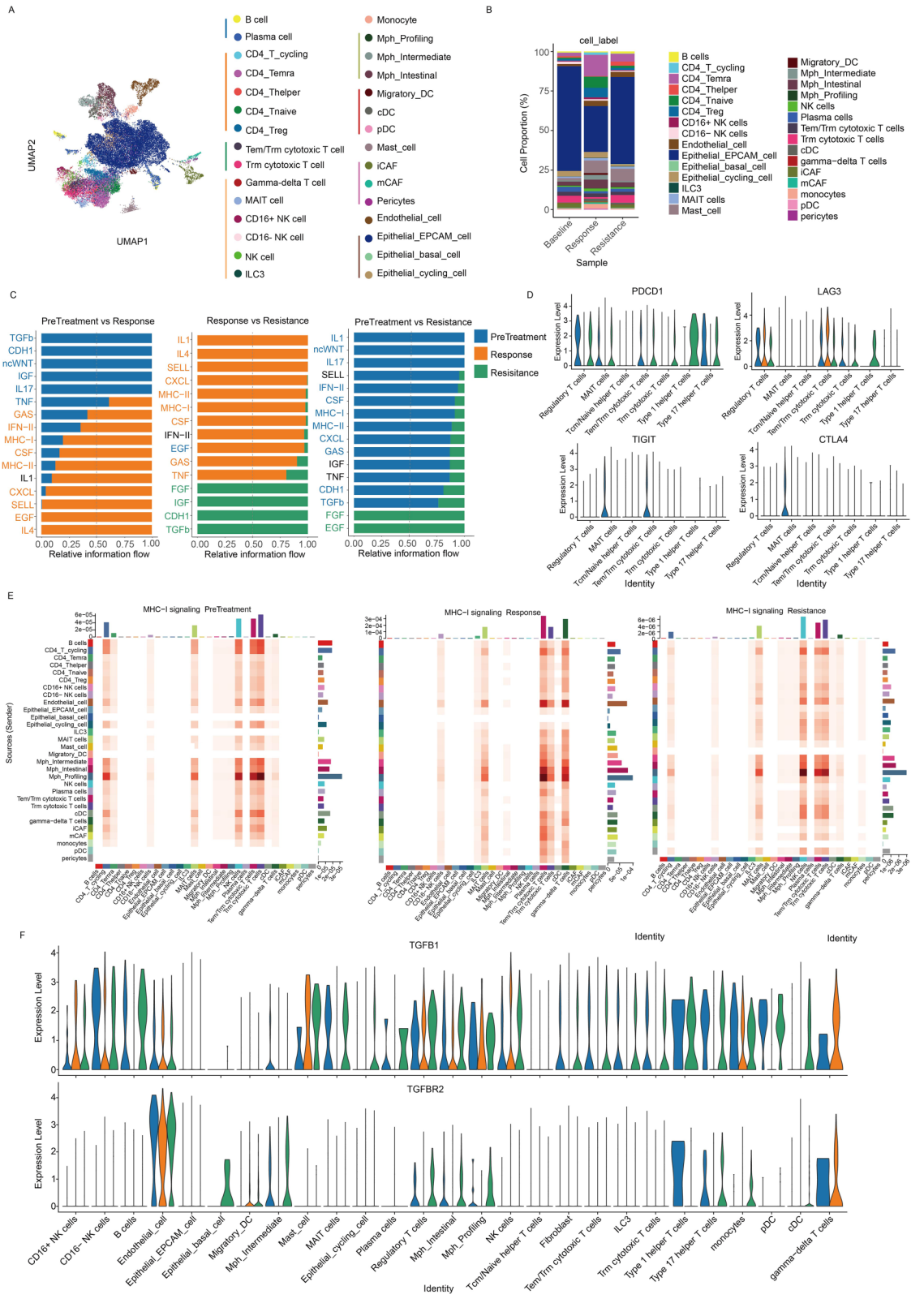

Figure 6 Cell communication in patients during pre-treatment, treatment response, and acquired resistance phases. (A) UMAP visualization of cellular distribution across baseline, response, and resistance phases, color-coded by cell labels. (B) Stacked bar plot displaying intra-sample cellular proportions. (C) RankNet plot comparing relative signaling pathway strengths, with green, orange, and blue denoting significant enrichment in baseline, response, and resistance phases, respectively. (D) Violin plot of common immune checkpoint expression levels in T-cell populations stratified by cell labels and phases. (E) Heatmap depicting the signaling activity patterns of the Major Histocompatibility Complex Class I (MHC-I) pathway across cell populations under three treatment phases. The color gradient (white to red) reflects the relative strength of signaling, with lighter tones indicating weaker activity and darker tones representing stronger activity. (F) Violin plot depicting Transforming Growth Factor-beta (TGF-β) signaling pathway expression dynamics across all cellular subsets and experimental phases.

sistance. Given its direct association with poor clinical outcomes, overcoming drug resistance is critical in both clinical practice and translational research. Recent advances in single-cell multi-omics sequencing have enabled the exploration of tumor heterogeneity at single-cell resolution. To the best of our knowledge, this is the first study utilizing single-cell sequencing data from a clinical cohort of Chinese patients to investigate the potential mechanisms of resistance to T-DXd. In this study, we systematically delineated the epithelial heterogeneity and TME remodeling underlying T-DXd resistance in advanced GC. Through comprehensive evaluation, MUC3A and CST3 expression was negatively correlated with the T-DXd response and was indentified as a novel biomarker for predicting outcomes in GC. These findings provide a valuable resource for enhancing our understanding of the mechanisms underlying T-DXd resistance and may facilitate the development of novel therapeutic targets to address this clinical challenge.

Our data strongly demonstrated that MUC3A was a key determinant of primary resistance to T-DXd in GC patients. Integrated analysis of gene expression signatures using scRNA-seq data nominated MUC3A as a candidate biomarker negatively associated with T-DXd response. Subsequent *in vitro* validation confirmed that downregulation of MUC3A enhanced cellular sensitivity to T-DXd in HER2-overexpressing GC cell lines. MUC3A is frequently overexpressed in GC and is correlated with tumor progression, advanced pathological features, and poor prognosis [29]. While previous studies have demonstrated that MUC family members mediate resistance to trastuzumab, with MUC1 promoting resistance through cytoplasmic domain-dependent PI3K/AKT activation and metabolic reprogramming whereas MUC4 confers resistance by masking HER2 epitopes to impair trastuzumab binding and inhibit antibody-dependent cellular cytotoxicity (ADCC) [24, 30], the role of MUC3A in T-DXd resistance remains unexplored. A study by Xu *et al*. reported that MUC3A can activate the PI3K/AKT/mmechanistic target of rapamycin (mTOR) pathway to promote the malignant phenotype of GC, while knockdown of MUC3A can block the PI3K/AKT pathway [31, 32]. Given that aberrant activation of the PI3K/Akt pathway is a key mechanism underlying resistance to HER2–targeted agents, we hypothesize that MUC3A may contribute to primary resistance to T–DXd by activating the PI3K/Akt pathway. Furthermore, we investigated whether MUC3A influences the binding of T–DXd to HER2 *in vitro*. Our results demonstrated that silencing MUC3A enhanced the binding of T–DXd to the HER2 epitope, suggesting that MUC3A may sterically hinder HER2 recognition, thereby impairing the binding efficiency and therapeutic efficacy of T–DXd. Notably, patients with low MUC3A expression showed a trend toward greater benefit from T-DXd, suggesting that the expression level of MUC3A may serve as an additional criterion to optimize treatment selection. Moreover, MUC3A expression levels can be readily assessed using various technology platforms, supporting its clinical feasibility. Analysis of an independent cohort of trastuzumab-treated patients also revealed that high MUC3A expression was significantly associated with shorter PFS, suggesting that MUC3A overexpression may represent a common mechanism limiting the efficacy of HER2-directed agents, including both T-DXd and trastuzumab. Collectively, our data strongly establish MUC3A as a key mediator of T-DXd resistance in GC and highlight its potential as both a novel predictive biomarker and a promising therapeutic target for overcoming resistance in HER2-positive GC.

Patients inevitably develop resistance during treatment, even after an initial response, thereby limiting the therapeutic benefits. The efficacy of T-DXd relies on efficient lysosomal delivery and enzymatic cleavage to release its cytotoxic payload, DXd. Although lysosomal dysfunction is a known resistance mechanism against T-DM1 [33–35], its role in T-DXd resistance in GC remains unclear. Notably, single-cell sequencing revealed progressively elevated CST3 expression during T-DXd treatment, which was validated using mIHC in paired tumor samples. CST3 naturally inhibits cysteine proteases like CTSB, which are responsible for cleaving the linker and releasing the payload from T-DXd [36, 37]. Elevated CST3 levels impaired proteolytic processing and payload release, thereby reducing T-DXd cytotoxicity. Functional validation demonstrated that CTSB knockdown conferred resistance to T-DXd in GC cells, whereas CST3 knockdown enhanced the drug sensitivity, supporting the proposed mechanism. To the best of our knowledge, this is the first study showing that CST3 overexpression contributes to T-DXd resistance in GC, providing important insights for future therapeutic development. In alignment with previous research identifying TGF-β as a direct transcriptional inducer of CST3 [38], we observed dynamic changes in TGF-β pathway activity throughout T-DXd treatment. Specifically, TGF-β signaling was suppressed during the initial response phase but was subsequently upregulated upon the development of acquired resistance. Based on this correlative pattern, we hypothesize that TGF-β signaling may serve as a key upstream regulator of CST3 expression following T-DXd treatment, although the precise mechanistic details require further validation. Consistent with previous findings, we found a marked decrease in HER2 expression levels in tumor cell populations from acquired resistance samples compared with baseline samples, highlighting the importance of dynamically monitoring HER2 status throughout therapy [39]. Moreover, accumulating evidence suggests that HER2 mutations, along with the associated signaling activation, may play a functional role in immune regulation [40]. Furthermore, resistant tumor cells exhibited marked downregulation of G_2/M checkpoint and cell-cycle genes, facilitating checkpoint bypass and sustained proliferation. This aligns with studies identifying cell cycle/DNA repair pathways as actionable targets in T-DXd-resistant breast cancer [41], underscoring the potential of cell-cycle-targeted strategies to overcome T-DXd resistance in GC.

Dynamic crosstalk between the TME and cancer cells is a pivotal mechanism underlying resistance to therapy. Extensive studies have demonstrated that hyperactivation of TGF-β signaling within the TME drives immune evasion by suppressing T-cell/NK-cell activity while remodeling the TME to promote tumor progression and therapy resistance [42]. PD-1, which is predominantly expressed on activated T and NK cells, suppresses multiple phases of the antitumor immune response and functions as a pivotal regulator of both adaptive and innate immunity in cancer [43, 44]. Clinical trials evaluating the combination of trastuzumab or T-DM1 with PD-1 blockade have revealed clinically meaningful enhancement in patient outcomes across multiple tumor types [45–47]. In our study, CellChat analysis of the TME revealed that initial T-DXd treatment upregulates MHC-I/II–mediated antigen presentation and increases secretion of pro-inflammatory cytokines (e.g. IFN-γ), thereby creating an immunologically activated microenvironment. However, sustained therapeutic pressure drives adaptive immunosuppressive reprogramming of the TME, marked by impaired antigen presentation, re-

activation of TGF-β signaling, and upregulation of FGF/EGF pathways. Concomitantly, we observed higher PD-1 levels on tumor-infiltrating immune cells, and the binding of PD-1 to its ligand programmed cell death ligand 1 (PD-L1) likely leads to effector cell exhaustion, helping tumors evade the immune response. These findings suggested that the emergence of T-DXd resistance in GC may be driven, in part, by dynamic TME-mediated immune evasion mechanisms. It has been reported that trastuzumab treatment can lead to the excessive secretion of TGF-β and IFN-γ. These two factors upregulate PD-L1 on tumor cells and PD-1 on NK cells, thereby inhibiting the cytotoxicity of NK cells and promoting immune escape and drug resistance. Furthermore, the TGF-β signaling pathway plays a critical role in regulating cell survival and proliferation. Its aberrant activation can significantly enhance the epithelial–mesenchymal transition process, ultimately contributing to trastuzumab resistance. Nevertheless, the precise mechanisms by which the TGF-β and PD-1/PD-L1 pathways mediate T-DXd resistance in GC remain largely unknown, necessitating further investigation. Taken together, prospective immunotherapeutic strategies aimed at targeting immune escape, such as intervention involving the PD-1 and TGF-β pathways, could offer a novel and promising clinical approach for patients resistant to T-DXd.

T-DXd has revealed a promising effect in GC patients with HER2 overexpression. Furthermore, our study constructed a detailed cellular atlas of GC during T-DXd therapy, delineated cell subpopulations and genes associated with resistance, and explored the complex interactions between tumor cells and their microenvironment. These insights shed light on the molecular underpinnings of T-DXd resistance. Specifically, we identified high MUC3A expression as a key driver of T-DXd resistance and a biomarker of poor prognosis, thereby highlighting its clinical relevance as a prognostic biomarker. Moving forward, refining patient selection and developing rational combination therapies are expected to further improve survival outcomes for GC patients.

Our study has several limitations. The relatively small sample size, due to the clinical context where T-DXd is currently approved as third-line therapy for HER2-positive GC following progression on trastuzumab-based regimens, may incompletely capture the inter-tumor heterogeneity and microenvironmental differences. Validation in larger cohorts is warranted to confirm the broad applicability of these conclusions. Additionally, regarding the exploratory TME analysis, we intend to further evaluate the therapeutic potential of combining T-DXd with PD-1/PD-L1 inhibitors and anti-TGF-β agents through expanded clinical cohorts and preclinical animal models, with the objective of enhancing clinical efficacy.

Acknowledgments

The authors gratefully thank all the patients for participating in this study. Funding support for the study was provided by the Beijing Xisike Clinical Oncology Research Foundation (No. Y-2022HER2AZMS-0377 to Z.P.), Beijing Natural Science Foundation (grant number 7242088 to X.W.), and the National Natural Science Foundation of China (grant number 82473050 to X.W.). The funders played no role in study design, data collection, analysis and interpretation of data, or the writing of this manuscript.

Author contributions

Bohan Zhang (Investigation, Software, Validation, Visualization, Writing— original draft, Writing— review & editing), Lei Zhang (Formal Analysis, Software), Cheng Liu (Supervision), Tong Xie (Writing— review & editing), Yifan Zhang (Writing— review & editing), Xiao Wu (Writing—review & editing), Yining Chen (Writing—review & editing), Siyuan Cheng (Writing—review & editing), Yang Feng (Writing—review & editing), Yuxin Wang (Writing—review & editing), Erke Gao (Writing—review & editing), Hongquan Zhang (Writing—review & editing), Lin Shen (Resources, Writing—review & editing), Zhi Peng (Funding acquisition, Project administration, Supervision, Writing—review & editing), Xiaofan Wei (Methodology, Supervision, Writing—review & editing).

Supplementary material

Supplementary material is available at *PCMEDI* online.

Conflicts of interest

The authors disclose no potential conflicts of interest. L.Z. is an employee of Burning Rock Biotech. The research presented in this manuscript was conducted independently and was not funded, sponsored, or directly supported by Burning Rock Biotech.

Ethics statement

This study was approved by the Ethics Committee of Peking University Cancer Hospital in 2021 (approval number: 2021YW90). Informed content was obtained from all patients enrolled for the collection of clinical information and samples, and all tests and procedures were conducted in accordance with the Declaration of Helsinki.

Data availability

The single-cell RNA sequencing data generated in this study is deposited at the Genome Sequence Archive for Humans with project number HRA012249. All relevant data supporting the key findings of this study are available within the article or from the corresponding author upon reasonable request.

References

1 Bray F, Laversanne M, Sung H *et al.* Global cancer statistics 2022: GLOBOCAN estimates of incidence and mortality worldwide for 36 cancers in 185 countries. *CA Cancer J Clin* 2024;**74**:229–63.

2 Suh YS, Na D, Lee JS *et al.* Comprehensive molecular characterization of adenocarcinoma of the gastroesophageal junction between esophageal and gastric adenocarcinomas. *Ann Surg* 2022;**275**:706–17. https://doi.org/10.1097/SLA.0000000000004303.

3 Huang D, Lu N, Fan Q *et al.* HER2 status in gastric and gastroesophageal junction cancer assessed by local and central laboratories: Chinese results of the HER-EAGLE study. *PLoS*

One 2013;**8**:e80290. https://doi.org/10.1371/journal.pone.0080290.
4 Sheng WQ, Huang D, Ying JM *et al.* HER2 status in gastric cancers: a retrospective analysis from four Chinese representative clinical centers and assessment of its prognostic significance. *Ann Oncol* 2013;**24**:2360–4. https://doi.org/10.1093/annonc/mdt232.
5 Bang YJ, Van Cutsem E, Feyereislova A *et al.* Trastuzumab in combination with chemotherapy versus chemotherapy alone for treatment of HER2-positive advanced gastric or gastro-oesophageal junction cancer (ToGA): a phase 3, open-label, randomised controlled trial. *Lancet* 2010;**376**:687–97. https://doi.org/10.1016/S0140-6736(10)61121-X.
6 Wang S, Zhao Y, Song Y *et al.* ERBB2D16 Expression in HER2 positive gastric cancer is associated with resistance to Trastuzumab. *Front Oncol* 2022;**12**:855308. https://doi.org/10.3389/fonc.2022.855308.
7 Miranda F, Prazeres H, Mendes F *et al.* Resistance to endocrine therapy in HR + and/or HER2 + breast cancer: the most promising predictive biomarkers. *Mol Biol Rep* 2022;**49**:717–33. https://doi.org/10.1007/s11033-021-06863-3.
8 Swain SM, Shastry M, Hamilton E. Targeting HER2-positive breast cancer: advances and future directions. *Nat Rev Drug Discov* 2023;**22**:101–26. https://doi.org/10.1038/s41573-022-00579-0.
9 Liu W, Chang J, Liu M *et al.* Quantitative proteomics profiling reveals activation of mTOR pathway in trastuzumab resistance. *Oncotarget* 2017;**8**:45793–806. https://doi.org/10.18632/oncotarget.17415.
10 Li Z, Zhao H, Hu H *et al.* Mechanisms of resistance to trastuzumab in HER2-positive gastric cancer. *Chin J Cancer Res* 2024;**36**:306–21. https://doi.org/10.21147/j.issn.1000-9604.2024.03.07.
11 Verma S, Miles D, Gianni L *et al.* Trastuzumab emtansine for HER2-positive advanced breast cancer. *N Engl J Med* 2012;**367**:1783–91. https://doi.org/10.1056/NEJMoa1209124.
12 Thuss-Patience PC, Shah MA, Ohtsu A *et al.* Trastuzumab emtansine versus taxane use for previously treated HER2-positive locally advanced or metastatic gastric or gastro-oesophageal junction adenocarcinoma (GATSBY): an international randomised, open-label, adaptive, phase 2/3 study. *Lancet Oncol* 2017;**18**:640–53. https://doi.org/10.1016/S1470-2045(17)30111-0.
13 Hunter FW, Barker HR, Lipert B *et al.* Mechanisms of resistance to trastuzumab emtansine (T-DM1) in HER2-positive breast cancer. *Br J Cancer* 2020;**122**:603–12. https://doi.org/10.1038/s41416-019-0635-y.
14 Baah S, Laws M, Rahman KM. Antibody-drug conjugates-A tutorial review. *Molecules* 2021;**26**:2943. https://doi.org/10.3390/molecules26102943.
15 Nakada T, Masuda T, Naito H *et al.* Novel antibody drug conjugates containing exatecan derivative-based cytotoxic payloads. *Bioorg Med Chem Lett* 2016;**26**:1542–5. https://doi.org/10.1016/j.bmcl.2016.02.020.
16 Khoury R, Saleh K, Khalife N *et al.* Mechanisms of resistance to antibody-drug conjugates. *Int J Mol Sci* 2023;**24**:9674. https://doi.org/10.3390/ijms24119674.
17 Meric-Bernstam F, Makker V, Oaknin A *et al.* Efficacy and safety of Trastuzumab Deruxtecan in patients with HER2-expressing solid tumors: primary results from the DESTINY-PanTumor02 Phase II trial. *J Clin Oncol* 2024;**42**:47–58. https://doi.org/10.1200/JCO.23.02005.
18 Shen L, Chen P, Lu J *et al.* Trastuzumab deruxtecan (T-DXd) in Chinese patients (pts) with previously treated HER2-positive locally advanced/metastatic gastric cancer (GC) or gastroesophageal junction adenocarcinoma (GEJA): primary efficacy and safety from the phase II single-arm DESTINY-Gastric06 (DG06) trial. *Ann Oncol* 2023;**34**:S1542–3.
19 Peng Z, Chen P, Lu J *et al.* Trastuzumab deruxtecan in patients from China with previously treated human epidermal growth factor receptor 2-positive locally advanced/metastatic gastric or gastroesophageal junction adenocarcinoma (DESTINY-Gastric06): results from a single-arm, multicenter, phase 2 trial. *EClinicalMedicine* 2025;**87**:103404.
20 Vanauberg D, Schulz C, Lefebvre T. Involvement of the pro-oncogenic enzyme fatty acid synthase in the hallmarks of cancer: a promising target in anti-cancer therapies. *Oncogenesis* 2023;**12**:16. https://doi.org/10.1038/s41389-023-00460-8.
21 Wang J, Sun N, Kunzke T *et al.* Metabolic heterogeneity affects trastuzumab response and survival in HER2-positive advanced gastric cancer. *Br J Cancer* 2024;**130**:1036–45. https://doi.org/10.1038/s41416-023-02559-6.
22 Chang J, Wang Q, Bhetuwal A *et al.* Metabolic pathways underlying GATA6 regulating trastuzumab resistance in Gastric Cancer cells based on untargeted metabolomics. *Int J Med Sci* 2020;**17**:3146–64. https://doi.org/10.7150/ijms.50563.
23 Liu J, Pan C, Guo L *et al.* A new mechanism of trastuzumab resistance in gastric cancer: MACC1 promotes the Warburg effect via activation of the PI3K/AKT signaling pathway. *J Hematol Oncol* 2016;**9**:76. https://doi.org/10.1186/s13045-016-0302-1.
24 Chen AC, Migliaccio I, Rimawi M *et al.* Upregulation of mucin4 in ER-positive/HER2-overexpressing breast cancer xenografts with acquired resistance to endocrine and HER2-targeted therapies. *Breast Cancer Res Treat* 2012;**134**:583–93. https://doi.org/10.1007/s10549-012-2082-9.
25 Diaz-Rodriguez E, Gandullo-Sanchez L, Ocana A *et al.* Novel ADCs and strategies to overcome resistance to anti-HER2 ADCs. *Cancers (Basel)* 2021;**14**:154. https://doi.org/10.3390/cancers14010154.
26 Tarantino P, Carmagnani Pestana R, Corti C *et al.* Antibody-drug conjugates: smart chemotherapy delivery across tumor histologies. *CA Cancer J Clin* 2022;**72**:165–82.
27 Zhou Y, Dong W, Wang L *et al.* Cystatin C attenuates perihematomal secondary brain injury by inhibiting the cathepsin B/NLRP3 signaling pathway in a rat model of intracerebral hemorrhage. *Mol Neurobiol* 2024;**61**:9646–62. https://doi.org/10.1007/s12035-024-04195-4.
28 Modenbach JM, Moller C, Asgarbeik S *et al.* Biochemical analyses of cystatin-C dimers and cathepsin-B reveals a trypsin-driven feedback mechanism in acute pancreatitis. *Nat Commun* 2025;**16**:1702. https://doi.org/10.1038/s41467-025-56875-x.
29 Xu J, Qiu J. Mucin 3A's promotion of the proliferation and migration of gastric cancer cells through activation of the mTOR pathway. *Altern Ther Health Med* 2025;**31**:155–61.
30 Lee DH, Choi S, Park Y *et al.* Mucin1 and Mucin16: therapeutic targets for cancer therapy. *Pharmaceuticals (Basel)* 2021;**14**:1053. https://doi.org/10.3390/ph14101053.

31 Xu J, Qiu J. Mucin 3A's promotion of the proliferation and migration of gastric cancer cells through activation of the mTOR pathway. *Altern Ther Health Med* 2025;**31**:155–61.

32 Luo Y, Ma S, Sun Y *et al.* MUC3A induces PD-L1 and reduces tyrosine kinase inhibitors effects in EGFR-mutant non-small cell lung cancer. *Int J Biol Sci* 2021;**17**:1671–81. https://doi.org/10.7150/ijbs.57964.

33 Rios-Luci C, Garcia-Alonso S, Diaz-Rodriguez E *et al.* Resistance to the antibody-drug conjugate T-DM1 is based in a reduction in lysosomal proteolytic activity. *Cancer Res* 2017;**77**:4639–51. https://doi.org/10.1158/0008-5472.CAN-16-3127.

34 Wang H, Wang W, Xu Y *et al.* Aberrant intracellular metabolism of T-DM1 confers T-DM1 resistance in human epidermal growth factor receptor 2-positive gastric cancer cells. *Cancer Sci* 2017;**108**:1458–68. https://doi.org/10.1111/cas.13253.

35 Kinneer K, Meekin J, Tiberghien AC *et al.* SLC46A3 as a potential predictive biomarker for antibody-drug conjugates bearing noncleavable linked maytansinoid and pyrrolobenzodiazepine warheads. *Clin Cancer Res* 2018;**24**:6570–82. https://doi.org/10.1158/1078-0432.CCR-18-1300.

36 Caculitan NG, Dela Cruz Chuh J, Ma Y *et al.* Cathepsin B is dispensable for cellular processing of Cathepsin B-cleavable antibody-drug conjugates. *Cancer Res* 2017;**77**:7027–37. https://doi.org/10.1158/0008-5472.CAN-17-2391.

37 Sun B, Zhou Y, Halabisky B *et al.* Cystatin C-cathepsin B axis regulates amyloid beta levels and associated neuronal deficits in an animal model of Alzheimer's disease. *Neuron* 2008;**60**:247–57. https://doi.org/10.1016/j.neuron.2008.10.001.

38 Solem M, Rawson C, Lindburg K *et al.* Transforming growth factor beta regulates cystatin C in serum-free mouse embryo (SFME) cells. *Biochem Biophys Res Commun* 1990;**172**:945–51. https://doi.org/10.1016/0006-291X(90)90767-H.

39 Mosele F, Deluche E, Lusque A *et al.* Trastuzumab deruxtecan in metastatic breast cancer with variable HER2 expression: the phase 2 DAISY trial. *Nat Med* 2023;**29**:2110–20. https://doi.org/10.1038/s41591-023-02478-2.

40 Attalla SS, Boucher J, Proud H *et al.* HER2Delta16 Engages ENPP1 to promote an immune-cold microenvironment in breast cancer. *Cancer Immunol Res* 2023;**11**:1184–202. https://doi.org/10.1158/2326-6066.CIR-22-0140.

41 Lee J, Kida K, Koh J *et al.* The DNA repair pathway as a therapeutic target to synergize with trastuzumab deruxtecan in HER2-targeted antibody-drug conjugate-resistant HER2-overexpressing breast cancer. *J Exp Clin Cancer Res* 2024;**43**:236. https://doi.org/10.1186/s13046-024-03143-3.

42 Batlle E, Massague J. Transforming growth factor-beta signaling in immunity and cancer. *Immunity* 2019;**50**:924–40. https://doi.org/10.1016/j.immuni.2019.03.024.

43 Ahmadzadeh M, Johnson LA, Heemskerk B *et al.* Tumor antigen-specific CD8 T cells infiltrating the tumor express high levels of PD-1 and are functionally impaired. *Blood* 2009;**114**:1537–44. https://doi.org/10.1182/blood-2008-12-195792.

44 Yang M, Lin W, Huang J *et al.* Novel immunotherapeutic approaches in gastric cancer. *Precis Clin Med* 2024;**7**:pbae020. https://doi.org/10.1093/pcmedi/pbae020.

45 Janjigian YY, Kawazoe A, Bai Y *et al.* Pembrolizumab plus trastuzumab and chemotherapy for HER2-positive gastric or gastro-oesophageal junction adenocarcinoma: interim analyses from the phase 3 KEYNOTE-811 randomised placebo-controlled trial. *Lancet* 2023;**402**:2197–208. https://doi.org/10.1016/S0140-6736(23)02033-0.

46 Loi S, Giobbie-Hurder A, Gombos A *et al.* Pembrolizumab plus trastuzumab in trastuzumab-resistant, advanced, HER2-positive breast cancer (PANACEA): a single-arm, multicentre, phase 1b-2 trial. *Lancet Oncol* 2019;**20**:371–82. https://doi.org/10.1016/S1470-2045(18)30812-X.

47 Li X, Zhang X, Yin S *et al.* Challenges and prospects in HER2-positive breast cancer-targeted therapy. *Crit Rev Oncol Hematol* 2025;**207**:104624. https://doi.org/10.1016/j.critrevonc.2025.104624.

Received: 26 October 2025. **Revised:** 10 December 2025. **Accepted:** 17 December 2025